



Heterodyne Brillouin microscopy for biomechanical imaging

MICHAEL A. TAYLOR,*  AMANDA W. KIJAS, ZHAO WANG, JAN LAUKO, AND ALAN E. ROWAN

Australian Institute for Bioengineering and Nanotechnology, The University of Queensland, St. Lucia, Queensland 4072, Australia

*m.taylor@sbs.uq.edu.au

Abstract: Microscopic variations in material stiffness play a vital role in cellular scale biomechanics, but are difficult to measure in a natural 3D environment. Brillouin microscopy is a promising technology for such applications, providing non-contact label-free measurement of longitudinal modulus at microscopic resolution. Here we develop heterodyne detection to measure Brillouin scattering signals in a confocal microscope setup, providing sensitive detection with excellent frequency resolution and robust operation in the presence of stray light. The functionality of the microscope is characterized and validated, and the imaging capability demonstrated by imaging structure within both a fibrin fiber network and live cells.

© 2021 Optical Society of America under the terms of the [OSA Open Access Publishing Agreement](#)

1. Introduction

The mechanical interaction of a cell with its surroundings is crucial to cell mobility [1], growth [2], metabolism [2], and can direct cell fate [3,4]. As such, accurate high-resolution mapping of mechanical properties within cells and the extracellular matrix that surrounds them holds great value for the study of cellular biomechanics. While much work has used atomic force microscopes [5], this technique requires physical access and thereby limits measurement to cells on a flat surface. This in turn provides a highly unnatural biomechanical environment that can completely alter normal cell movement and responses, thus undermining the relevance of the data obtained in this context [6].

Brillouin microscopy is an emerging technology which can provide noncontact 3D elastography at microscopic resolution [7–10]. Brillouin microscopes rely on Brillouin light scattering in which light scatters from acoustic waves [11]. This scattering allows measurement of both the local sound velocity and attenuation at microscopic scale (Fig. 1(a)), which relates to the complex longitudinal modulus. The longitudinal modulus relates to the material compressibility, and is not directly relatable to the Young's modulus as measured with methods such as atomic force microscopy [12]. The simplest and most common approach to Brillouin microscopy uses spontaneous Brillouin scattering, in which the acoustic waves are generated by thermal fluctuations. This allows biomechanical measurements using only a single input laser field in a confocal microscope. Another approach is to use optical fields to generate the acoustic waves, as used in either stimulated Brillouin microscopy [13,14] or impulsive Brillouin microscopy [15,16]. While these two techniques offer an advantage in sensitivity and speed, they require multiple laser fields to interact from different input directions, and hence are constructed with dual microscope objectives which increases the cost and complexity of the system and makes it incompatible with the standard sample preparations used in confocal microscopy.

The key challenge to Brillouin microscopy is the ability to detect a very small signal, for example, 10^{-11} of the input power for spontaneous Brillouin scattering in water [7,11]. Furthermore, the frequency shift of Brillouin scattering is a few GHz which is only detectable with extremely fine spectral resolution. The two approaches which have been previously used are tandem Fabry-Perot interferometers (TFPI), which act as a narrow band-pass filter that is scanned over the

spectral range, and virtually imaged phase array (VIPA) spectrometers which act as a dispersive element separating the range of frequencies onto different pixels of a camera [7,9]. TFPI offer superior spectral resolution and isolation of stray background light, while VIPA operate at far higher speed and require less total light flux due to the parallel simultaneous measurement of all frequencies [17]. The speed offered by VIPA has been particularly valuable for imaging the Brillouin shifts in cells and in animals [9,18–20], while the resolution of TFPI has enabled more precise measurements such as the full elastic tensor of spider silk [21,22].

Here we introduce heterodyne spectroscopic detection for Brillouin microscopy, which allows parallel detection with extremely fine spectral resolution. Heterodyne detection is a well-established method, and has previously been applied to measure Brillouin scattering in optical fibers [23–25]. Our system introduces heterodyne detection of Brillouin scattering into microscopy, and using GHz bandwidth detection and signal processing to greatly improve detection sensitivity and bandwidth. We characterize the microscope performance and demonstrate its use

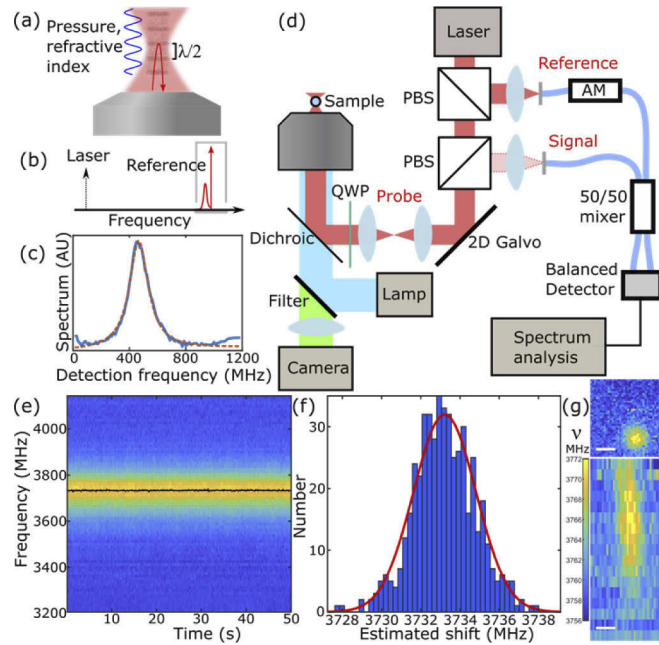


Fig. 1. Concept and validation. (a) Sound waves cause a periodic modulation of pressure and hence the refractive index, which causes Brillouin scattering of light when its period is half the optical wavelength. (b) Heterodyne detection measures the beat between the reference and the Brillouin scattered light, which allows us to shift the Brillouin signal into the detection bandwidth by selecting an appropriate reference frequency. (c) Example of a Brillouin scattered peak from water, measured with a 4200 MHz shifted reference (blue) with a Lorentzian fit (orange dashed). (d) Schematic layout of our experimental setup. QWP: Quarter wave plate, PBS: polarizing beamsplitter, AM: amplitude modulator. The microscope also incorporates fluorescence and transmission imaging to allow correlative multimodal measurements. (e) Spectrogram of 50 s of data recorded in water. The peak frequency (black line) is estimated by fitting to the data. (f) Histogram of estimated Brillouin peaks. The variation has standard deviation of 1.6 MHz, or normalized $\Delta\bar{\nu} = 4.3 \times 10^{-4}$. (g) The resolution is estimated by spatially mapping the Brillouin shift around a 503 nm polystyrene nanosphere embedded in 3D, shown in xy (top) and xz (bottom), with 1 μm scale bars. The estimated resolution is 0.75 μm in x and y , and 4.2 μm in z .

to characterize Brillouin scattering to establish stiffness maps of complex 3D biological samples, fibrin fiber networks and live cells.

2. Method

In heterodyne detection a weak optical signal is amplified by its interference with a strong reference to achieve single-photon level sensitivity while requiring only basic and inexpensive detectors. The signal field is combined with a stronger reference field on a 50/50 beamsplitter, followed by balanced detection of the intensity at the two beamsplitter outputs (Fig. 1(d)). The resulting photocurrent is sensitive to the interference between the two fields, while remaining insensitive to fluctuations in the reference field intensity [26]. The spectrum is then determined via Fourier transform. The detected photocurrent corresponds to a beat at the frequency difference between signal and reference fields (Fig. 1(b), c). The frequency of this beat depends only on the Brillouin shift and not on the absolute frequency of the laser source, making it calibration-free and insensitive to drifts of the laser frequency. Drifts of the laser frequency do change the Brillouin scattering frequency, however this shift in Brillouin frequency is less than 10^{-14} of the laser drift, and can safely be neglected. By comparison, both TFPI and VIPA spectrometers measure the absolute frequency, such that frequency drifts of the laser are directly convolved with the Brillouin signal. While drifts can be addressed with active stabilization, this further increases the cost and complexity of the system [27]. Additionally, heterodyne detection provides Fourier-limited frequency resolution, limited only by the duration of the measurement. Here we choose 3.125 MHz frequency resolution, which is around 100 times narrower than typically achieved with VIPA spectrometers [9,19]. Note that the frequency resolution denotes the spacing between measurable frequencies in the Brillouin spectrum, and is not equivalent to the frequency precision, which is the accuracy with which the frequency of a single Brillouin peak can be estimated. Use of a narrower frequency resolution permits characterization of the Brillouin spectrum with a finer spacing between samples, but does not automatically provide finer frequency precision.

Our implementation uses 1064 nm laser light, which allows the use of inexpensive shot noise limited GHz detectors. The Brillouin scattering rate scales as λ^{-4} , which necessitates use of higher power than visible light. However, since photodamage is far lower in the infra-red, far higher power can be used before photodamage becomes a concern [10,28,29]. Damage in Brillouin microscopy has been quantified by the onset of visible blebbing [18], which showed that the highest nonlethal power for 1 hour exposure is around 800 μ W for 532 nm and 69 mW at 660 nm. The reduced damage at longer wavelength is expected because longer wavelengths carry less photon energy, and produce far less single photon photochemical disruption [28–31]. Even higher powers have been used in Brillouin microscopes operating in near infrared wavelength, with 265 mW used for live imaging without visible damage at 780 nm [14]. Based on this data, we used a comparable laser power of 276 mW in our live cell visualization experiments. We additionally monitored cell damage using NucGreen (ThermoFisher) fluorescent live/dead stain to confirm that the cells remain alive after imaging, thus demonstrating compatibility with living biological samples.

The heterodyne Brillouin measurement was incorporated into a custom made confocal microscope (Fig. 1(d), described in detail in Supplementary Information). The light is collected into a single-mode fiber, which acts to limit light collection to the focal spot in a similar way to a confocal pinhole [32], which is a common approach for confocal Brillouin microscopes [7,9,18]. The collected Brillouin signal is mixed with a frequency-shifted reference field, with the resulting interference detected on a 1 GHz bandwidth detector. While not strictly essential, the use of a frequency-shifted reference reduces the bandwidth required from the detector and digitizer as the GHz Brillouin scattered signal can be shifted towards the bandwidth of detection (Fig. 1(b), c)). Subsequently, the detected signal is converted to a digital power spectrum using a custom

built real-time spectrum analyzer housed in a National Instruments PXI system (Supplementary Information). Real-time spectrum analysis is necessary to capture all of the data within the detected signal in order to maximize sensitivity (Supplementary Information).

Next, we characterized the system noise performance, and the detection was found to be shot noise limited (Supp Fig. S1, [Supplement 1](#)). The noise contributions from adding excess light in the signal port was also evaluated, and the primary effect of additional background light was found to result in an increase in the shot noise floor (Supp Fig. S2, [Supplement 1](#)), which we subtract in subsequent data preprocessing. We find that measurements remain robust even with several microwatts of background power reaching the detector, which is over 6 orders of magnitude brighter than the Brillouin scattered signal. This intrinsic robustness alleviates the need for specialized filters to eliminate unscattered light, as is often required in VIPA-based Brillouin microscopes [27,33].

The longitudinal modulus M can be estimated from the Brillouin frequency ν_B , if both the refractive index n and mass density ρ are also known

$$M = \frac{\lambda \nu_B}{2n\rho^2 \sin\left(\frac{\theta}{2}\right)}$$

Here θ is the angle between incident and scattered light. In our case we do not have reliable *in situ* measurements of n and ρ , and hence do not estimate the longitudinal modulus. Similar to most papers in the field [7,9,14–16,18–20,34–36] we only report the Brillouin shift, and here follow the convention established at the recent COST Action BioBrillouin workshop [10] to parametrize the Brillouin parameters in normalized units.

3. Performance

An example spectra recorded in water with 345 mW power and 100 ms dwell time (Fig. 1(e), f) demonstrates the stability and precision of the measurement. Although the laser frequency is not stabilized, the raw data shows no shift over the course of 50 s. Once the data is acquired, the Brillouin peak frequency and linewidth is estimated using least squares fitting in a custom Matlab script (Supplementary Information). The estimated Brillouin shifts in water have an approximately Gaussian distribution with a standard deviation of 1.6 MHz (Fig. 1(f)), or $\Delta\bar{\nu} = 4.3 \times 10^{-4}$ when expressed in normalized units of $\bar{\nu} = \nu/\nu_W - 1$, with ν_W the measured Brillouin shift of water [10]. This precision is better than reported for either TFPI or VIPA Brillouin microscopes, though we achieve this at higher power than those reported results [10,18,34,37]. The peak signal-to-noise-ratio of this data is 81, for which the Cramér–Rao bound to Brillouin frequency estimation would be 1.4 MHz (see Supplementary Information). The variations in estimated Brillouin frequency only exceeds the predicted precision limit by a factor of 1.14.

The microscope resolution was characterized by spatially mapping the Brillouin shift around a 503 nm polystyrene nanosphere (Bangs Labs, FSPP003) embedded in 3D polyisocyanopeptide hydrogel (Fig. 1(g)). The resolution was estimated from the area in which Brillouin scattering frequency was increased around the bead location, which had a full width half-maximum of 0.90 μm in x and y , and 4.2 μm along the z axis. Resolution in confocal microscopes is commonly estimated by imaging sub-wavelength fluorescent nanospheres. Here we used a relatively large size as Brillouin scattering cannot be highly localized [38], which slightly broadens the spot size. Accounting for the bead size, the estimated resolution is 0.75 μm in x and y , and 4.2 μm along the z axis, consistent with diffraction-limited imaging with an effective numerical aperture of 0.67.

Measurement precision was characterized in water for a range of probe powers and pixel dwell times (Supp Fig. S3, [Supplement 1](#)). The precision of Brillouin shift estimates scales as the inverse square root of pixel dwell time, similar to other shot noise limited Brillouin measurements. Unlike other measurements, the precision scales inversely with the probe power reaching the sample. This is because heterodyne detection has different noise characteristics

to photon counting measurement. At the shot noise limit photon counting measurements have variance equal to the photon number N , while heterodyne detection has an additional constant noise floor that persists even in the absence of any signal (Supplementary Notes 2, 3, [Supplement 1](#)). While this has negligible effect where the signal is strong, it leads to poorer sensitivity in the limit that fewer than one photon scatters within the coherence time of the source. This means that photon counting measurements will be more suitable than heterodyne detection for signals with extremely low photon number such as in Brillouin scattering from shear waves [21].

Increasing the probe power was found to increase the Brillouin shift, consistent with laser heating (Supp Fig. S4, [Supplement 1](#)). Using the temperature dependence of the speed of sound, we estimated that the laser caused 27.5 K/W of heating. Optical heating from 1064 nm lasers has previously been studied for optical tweezers, and a lower heating rate of 8 K/W was reported [39]. Part of this discrepancy may be due to the nature of the measurement, as optical tweezers have a trapped microsphere at the laser focus and are sensitive to the water directly surrounding this sphere, while here we are sensitive to the water at the most intense part of the focus.

We measured the speed at which the laser generated heating by measuring the Brillouin shift in water after opening the laser shutter (Supp Fig. S5, [Supplement 1](#)). The water should initially be at room temperature, and its temperature increases once the laser is incident. The Brillouin shift was measured with 1 ms temporal resolution, and it was found that spectra measured within 1 ms of the shutter opening already exhibit most of the laser heating seen over a long timescale. This indicates that the majority of laser heating occurs at a sub-millisecond timescale. The rapid speed is consistent with results from plasmonic sensing, where the majority of heating has been measured to occur within 70 μ s [40]. Finer temporal resolution could in principle reveal the dynamics of the heating, but was not achievable here due to the timing jitter of the optical shutter and its 3 ms specified time to open.

In experiments where this heating is unacceptable, it can be reduced by using D₂O heavy water which has minimal absorption at near infra-red wavelengths, which we find reduces the heating by an order of magnitude (Supp Fig. S4, [Supplement 1](#)). Heavy water has similarly been used in optical tweezers biophysics experiments to mitigate thermal damage [41,42]. The measurement shows that Brillouin scattering can be applied to estimate sample temperature at the focus. However, this approach is likely to be practical only in well-characterized materials where the temperature dependence of the speed of sound is well known.

The observation that heating can shift the Brillouin peak also raises a complication to the interpretation of Brillouin scattering data, as it demonstrates that changes in Brillouin shift can result not only from changes in material properties but also changes in temperature. As such any variation in optical absorption could change the optical heating, and introduce a non-mechanical variation in the Brillouin shift. This confounding influence should be considered in all Brillouin microscopes, and particularly those operating at high power such as used in stimulated and impulsive Brillouin microscopes [13–15].

Heterodyne measurement relies on the beat frequency between the reference and Brillouin scattered signal, which can correspond to signal frequencies either above or below the reference. To unambiguously localize the Brillouin shift, and to measure the Brillouin spectrum over a larger range than the detector bandwidth, we scan the reference frequency (Fig. 2(a), Supp Fig. S6 in [Supplement 1](#)). Measurement of the beat frequency at multiple reference frequencies allows unambiguous identification of any spectral features. Figure 2(a) shows the measured beat frequencies from Brillouin scattering in water as the reference frequency is varied between 3000 and 6000 MHz, which provides a measurement of the spectrum from 2000–7000 MHz.

We validated the Brillouin measurements by measuring water, isopropanol, acetone, methanol, and ethanol (Fig. 2(b)). The measured Brillouin frequency closely follows the expected value of $\nu = \frac{2nc_s}{\lambda}$, with c_s the speed of sound in the material, n the refractive index, and λ the vacuum wavelength (Fig. 2(c)). The measured Brillouin shifts span a 1.1 GHz range, with each shift

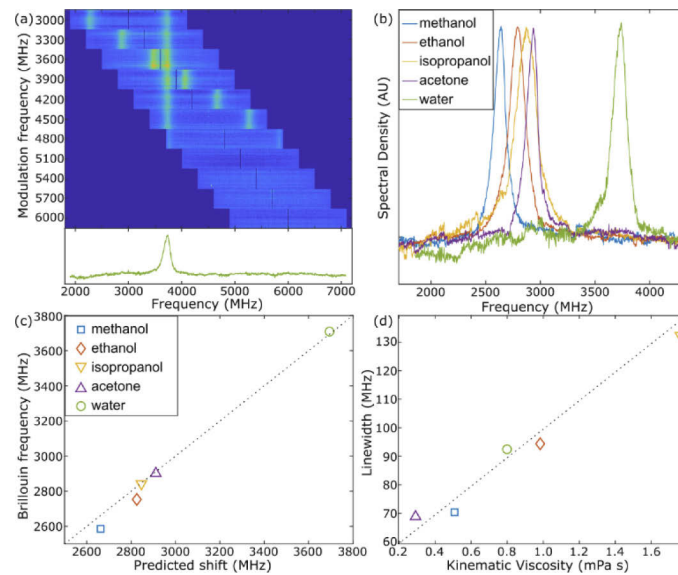


Fig. 2. (a) Brillouin scattering is measured with different reference frequencies. Signals either above or below the reference frequency both appear within the measurement bandwidth. Since the measurement does not distinguish between these, here we display each measured spectra both above and below the reference frequency. The Brillouin scattering peak at 3.7 GHz is observed consistently for any chosen reference frequency. By merging the data recorded at different reference frequencies we can infer the Brillouin scattering spectrum across a wide frequency range (line plot below, see Supplementary Fig. 5). (b) Brillouin spectra of methanol (blue), ethanol (red), isopropanol (yellow), acetone (purple) and water (green). Each peak has been scaled to the same height. (c) The extracted Brillouin shift follows closely the frequency that would be expected based on the sound velocity in each liquid (Supplementary Note 4). (d) Although the linewidth depends on both kinematic and bulk viscosity, we see a general trend of measured linewidth increasing with kinematic viscosity.

agreeing with the predicted value to within 3%. Discrepancies in sample temperature could account for the small discrepancies between measured and expected Brillouin frequencies, as we assumed each material to have comparable optical heating to water, which leads to a temperature of 30 °C (Supplementary Note 4). We further find that the linewidth correlates well to the material viscosity (Fig. 2(d)). The Brillouin linewidth depends on both kinematic and bulk viscosities, with the two viscosity types having comparable contributions to the linewidth [43]. Perfect correspondence cannot be expected as the bulk viscosity can vary separately from the kinematic viscosity (Supplementary Note 4, [Supplement 1](#)).

4. Imaging

The capacity for Brillouin imaging was demonstrated in two 3D biological samples, a fibrin hydrogel (Fig. 3(a)), whose fibrin fiber network imparts the key mechanical properties of a blood clot, as well as live cells within 3D growth matrices (Fig. 3(b)-(e)). The architecture of fibrin fiber networks can be quite diverse in structure, particularly the 3D branching and the pores this creates, but the network often has pore diameters larger than 5 μm [44]. We used a 4 mg/mL fibrin hydrogel with a pore size of 3.8 μm and an average fiber diameter of 420 nm (Supp Fig. S7, [Supplement 1](#)). The sensitivity of detection was sufficient to easily resolve individual fibers within the network, despite their size being smaller than the optical resolution of the microscope.

The stiffness of this fine 3D structure was mapped, with Brillouin shifts $\bar{\nu}$ covering the range of 0.014–0.025 relative to the Brillouin frequency of water. To the best of our knowledge this is first experiment to show the fiber structure of a biological hydrogel with Brillouin microscopy. Several previous works have characterized Brillouin scattering in hydrogels, though this has primarily been in fine mesh synthetic gels without resolving any spatial structure [7,9,12,16,45]. While Ref. [35] has shown some difference in the Brillouin scattering between pores and walls of gelatin methacrylate, they did not show individual filament structures.

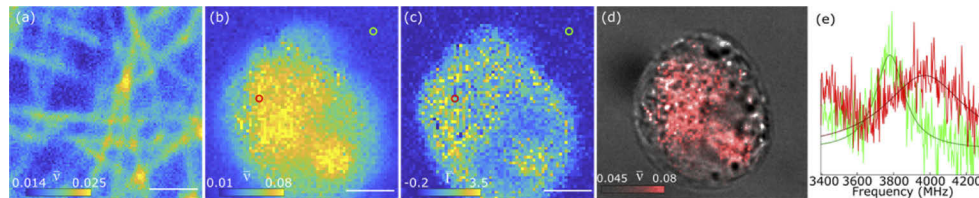


Fig. 3. Example images. (a) Normalized Brillouin shift for a fibrin hydrogel, for which we can resolve the individual fibers. To improve precision the dwell time here is 400 ms. The fibrin fibers are not resolved in the measured linewidths. (b) Normalized Brillouin shift and (c) linewidth for a single live HeLa cell cultured in a 3D environment, imaged with 276 mW and 100 ms dwell time. Some regions of high stiffness and high viscosity within the interior of the cell are visible, which likely correspond to nucleus and Golgi apparatus. (d) Overlay of the Brillouin shift on a transmission light image of the cell. (e) Example spectra from within the cell (red) and from the background (green). The increase in both frequency and linewidth is clearly visible. Around 2 μ W of excess light scattered by the cell contributes to the noise visible at low frequency. Scale bars: 5 μ m

Figure 3(b)–(e) shows Brillouin microscopy of live HeLa cells. HeLa cells were encapsulated within a 2 mg/mL polyisocyanopeptide hydrogel, which is a biomimetic synthetic gel previously employed in 3D cell cultures [4,46]. The image was acquired with 100×100 pixels with 100 ms dwell time, such that the 20 μ m square image was acquired in 1000 s. The HeLa cells showed an increase in both the Brillouin shift and linewidth throughout the cytosol, with some internal structures producing particularly high shifts. These extra stiff regions are expected to be larger organelles, and tentatively identified as the nucleus and Golgi apparatus due to their size and localization. The dynamic range was much greater within the cell (0.01–0.08) as reflected by the more complex organization of a cell.

The peak SNR is 25 in the background and 12 in the cell (Fig. 3(e)). This corresponds to an estimated limit to frequency precision $\Delta\bar{\nu}$ of 0.0007 in the background, and 0.002 within the cell. The reduced sensitivity within the cell is primarily due to the higher linewidth rather than the reduced SNR, as the precision of Brillouin frequency estimation increases with the linewidth (Supplementary Information).

As with most live cell imaging modalities [29], phototoxicity is a major concern. Brillouin microscopes are noted to cause sufficient photodamage to induce cell blebbing [9,18]. The compatibility of our microscope for live imaging of dynamic responses was confirmed both by monitoring the cell morphology, and by assessing cell viability during and after imaging with a NucGreen stain. This fluorescent marker only labels the nucleus of cells with compromised membranes, which indicates the cell to be fatally damaged. No fluorescence was seen after Brillouin imaging (Supp Fig. S8). As a positive control, we added ethanol to the imaged cell sample and then observed strong nuclear fluorescence after this chemical damage to the cells (Supp Fig. S8). The use of a cell death stain has been recommended as a control for all cellular Brillouin imaging experiments [10]. However, it should be noted that the stain only indicates

disruption of the cell membrane, while phototoxic damage can also show up as deficiencies in long-term development [29,31].

Optical heating could in principle contribute to the measured shifts seen here. The total effect from optical heating was estimated to be a frequency shift of $\bar{\nu} = 0.016$ and linewidth narrowing of $\bar{\Gamma} = -0.2$ (Supp Fig. S4). By comparison, the cell interior produced five times larger Brillouin shift (Fig. 3(b)) and with linewidth broadening rather than narrowing (Fig. 3(c)). We therefore rule out heating playing a primary role in the measured Brillouin shift in cells. However, it is possible that some proportion of the shift may be attributable to heating.

5. Outlook

Heterodyne detection provides an alternative method to detect Brillouin scattering, offering finer frequency resolution and background rejection than a VIPA spectrometer, and higher speed than a TFPI [10]. The absolute sensitivity demonstrated here is comparable to VIPA based spectrometers [9,10,19,27], but required higher power to achieve this. Compared to VIPA or TFPI detectors, heterodyne detection is relatively straightforward to implement. The experimental setup uses many similar parts to swept source optical coherence tomography (OCT) [47], which may provide an appropriate basis from which to build a heterodyne Brillouin microscope.

Our results show that laser heating can cause shifts in the Brillouin frequency. Since temperature directly influences the longitudinal modulus, all types of Brillouin microscope would be sensitive to heating. We suggest that temperature effects should be considered in more carefully in all Brillouin microscopes, and particularly those that use high power such as stimulated and impulsive Brillouin microscopes. It could be useful in future to combine Brillouin microscopy with fluorescent temperature indicators [48] that could measure the presence of laser heating, and allow estimation of spurious heating effects on the Brillouin shift.

In addition to applications in cell biology, which have been discussed in previous works [9,10,18,36], we consider Brillouin microscopy to be a promising method to characterize biological matrices. Biological hydrogel networks typically have pore sizes in the micron scale [1,44,49]. This allows the Brillouin shifts from highly supported branch points to be separated from the more flexible regions in between. This could provide useful information for understanding microscale variations in these networks which the usual rheology measurements of bulk stiffness fail to dissect. Further, when focusing the laser on a solid fiber we should observe a high concentration of solid material. This is important for separating solid contributions from the water, which is increasingly difficult at high levels of hydration [12]. At sufficiently high solid concentrations the Brillouin shift can coincide with relaxation frequencies, resulting in a resonant shift in the Brillouin peak [50]. With resolvable fibers this may be observable simply by scanning through different solid concentrations within the sample. We anticipate that this will be a valuable area for future investigation.

Funding. Australian Research Council (DE190100641, FL160100139); University of Queensland (Vice-Chancellor's Strategic Initiatives Fund).

Acknowledgments. We appreciate helpful discussions with Warwick Bowen, Elizabeth Bridge, and Nicolas Mauranyapin.

Disclosures. The authors declare no conflicts of interest.

Data Availability. Data underlying the results presented in this paper may be obtained from the authors upon reasonable request.

Supplemental document. See [Supplement 1](#) for supporting content.

References

1. H. C. Pruitt, D. Lewis, M. Ciccaglione, S. Connor, Q. Smith, J. W. Hickey, J. P. Schneck, and S. Gerecht, "Collagen fiber structure guides 3D motility of cytotoxic T lymphocytes," *Matrix Biol.* **85-86**, 147–159 (2020).
2. M. Urbanczyk, S. L. Layland, and K. Schenke-Layland, "The role of extracellular matrix in biomechanics and its impact on bioengineering of cells and 3D tissues," *Matrix Biol.* **85-86**, 1–14 (2020).

3. A. J. Engler, S. Sen, H. L. Sweeney, and D. E. Discher, "Matrix elasticity directs stem cell lineage specification," *Cell* **126**(4), 677–689 (2006).
4. R. K. Das, V. Gocheva, R. Hammink, O. F. Zouani, and A. E. Rowan, "Stress-stiffening-mediated stem-cell commitment switch in soft responsive hydrogels," *Nat. Mater.* **15**(3), 318–325 (2016).
5. K. Haase and A. E. Pelling, "Investigating cell mechanics with atomic force microscopy," *J. R. Soc. Interface.* **12**(104), 20140970 (2015).
6. B. M. Baker and C. S. Chen, "Deconstructing the third dimension—how 3D culture microenvironments alter cellular cues," *J. Cell Sci.* **125**, 3015–3024 (2012).
7. G. Scarcelli and S. H. Yun, "Confocal Brillouin microscopy for three-dimensional mechanical imaging," *Nat. Photon.* **2**(1), 39–43 (2008).
8. K. J. Koski and J. L. Yarger, "Brillouin imaging," *Appl. Phys. Lett.* **87**, 061903 (2005).
9. G. Scarcelli, W. J. Polacheck, H. T. Nia, K. Patel, A. J. Grodzinsky, R. D. Kamm, and S. H. Yun, "Noncontact three-dimensional mapping of intracellular hydromechanical properties by Brillouin microscopy," *Nat. Methods* **12**(12), 1132–1134 (2015).
10. G. Antonacci, T. Beck, A. Bilenca, J. Czarke, K. Elsayad, J. Guck, K. Kim, B. Krug, F. Palombo, and R. Prevedel, "Recent progress and current opinions in Brillouin microscopy for life science applications," *Biophys. Rev.* **12**(3), 615–624 (2020).
11. H. Z. Cummins and R. W. Gammon, "Rayleigh and Brillouin scattering in liquids: the Landau—Placzek ratio," *J. Chem. Phys.* **44**(7), 2785–2796 (1966).
12. P. J. Wu, I. V. Kabakova, J. W. Ruberti, J. M. Sherwood, I. E. Dunlop, C. Paterson, P. Torok, and D. R. Overby, "Water content, not stiffness, dominates Brillouin spectroscopy measurements in hydrated materials," *Nat. Methods* **15**(8), 561–562 (2018).
13. C. W. Ballmann, J. V. Thompson, A. J. Traverso, Z. Meng, M. O. Scully, and V. V. Yakovlev, "Stimulated Brillouin scattering microscopic imaging," *Sci. Rep.* **5**(1), 18139 (2016).
14. I. Remer, R. Shaashoua, N. Shemesh, A. Ben-Zvi, and A. Bilenca, "High-sensitivity and high-specificity biomechanical imaging by stimulated Brillouin scattering microscopy," *Nat. Methods* **17**(9), 913–916 (2020).
15. C. W. Ballmann, Z. Meng, A. J. Traverso, M. O. Scully, and V. V. Yakovlev, "Impulsive Brillouin microscopy," *Optica* **4**(1), 124 (2017).
16. B. Krug, N. Koukourakis, and J. W. Czarke, "Impulsive stimulated Brillouin microscopy for non-contact, fast mechanical investigations of hydrogels," *Opt. Express* **27**(19), 26910–26923 (2019).
17. Z. Coker, M. Troyanova-Wood, A. J. Traverso, T. Yakupov, Z. N. Utegulov, and V. V. Yakovlev, "Assessing performance of modern Brillouin spectrometers," *Opt. Express* **26**(3), 2400–2409 (2018).
18. M. Nikolić and G. Scarcelli, "Long-term Brillouin imaging of live cells with reduced absorption-mediated damage at 660 nm wavelength," *Biomed. Opt. Express* **10**(4), 1567–1580 (2019).
19. C. Bevilacqua, H. Sánchez-Iranzo, D. Richter, A. Diz-Muñoz, and R. Prevedel, "Imaging mechanical properties of sub-micron ECM in live zebrafish using Brillouin microscopy," *Biomed. Opt. Express* **10**(3), 1420–1431 (2019).
20. J. Zhang and G. Scarcelli, "Mapping mechanical properties of biological materials via an add-on Brillouin module to confocal microscopes," *Nat. Protoc.* **16**(2), 1251–1275 (2021).
21. K. J. Koski, P. Akhenblit, K. McKiernan, and J. L. Yarger, "Non-invasive determination of the complete elastic moduli of spider silks," *Nat. Mater.* **12**(3), 262–267 (2013).
22. D. Schneider, N. Gomopoulos, C. Y. Koh, P. Papadopoulos, F. Kremer, E. L. Thomas, and G. Fytas, "Nonlinear control of high-frequency phonons in spider silk," *Nat. Mater.* **15**(10), 1079–1083 (2016).
23. R. Shelby, M. Levenson, and P. Bayer, "Resolved forward Brillouin scattering in optical fibers," *Phys. Rev. Lett.* **54**(9), 939–942 (1985).
24. K. Shimizu, T. Horiguchi, Y. Koyamada, and T. Kurashima, "Coherent self-heterodyne detection of spontaneously Brillouin-scattered light waves in a single-mode fiber," *Opt. Lett.* **18**(3), 185–187 (1993).
25. H. Tanaka and T. Sonehara, "Superheterodyne Brillouin spectroscopy using frequency-tunable lasers," *Phys. B* **219-220**, 556–558 (1996).
26. W. P. Bowen and G. J. Milburn, *Quantum Optomechanics* (CRC, 2015).
27. Z. Meng, A. J. Traverso, C. W. Ballmann, M. A. Troyanova-Wood, and V. V. Yakovlev, "Seeing cells in a new light: a renaissance of Brillouin spectroscopy," *Adv. Opt. Photonics* **8**, 300 (2016).
28. K. C. Neuman, E. H. Chadd, G. F. Liou, K. Bergman, and S. M. Block, "Characterization of photodamage to *Escherichia coli* in optical traps," *Biophys. J.* **77**(5), 2856–2863 (1999).
29. R. Cole, "Live-cell imaging: the cell's perspective," *Cell. Adh. Migr.* **8**(5), 452–459 (2014).
30. M. A. Taylor and W. P. Bowen, "Quantum metrology and its application in biology," *Phys. Rep.* **615**, 1–59 (2016).
31. P. M. Carlton, J. Boulanger, C. Kervrann, J.-B. Sibarita, J. Salameiro, S. Gordon-Messer, D. Bressan, J. E. Haber, S. Haase, and L. Shao, "Fast live simultaneous multiwavelength four-dimensional optical microscopy," *Proc. Natl. Acad. Sci. USA* **107**(37), 16016–16022 (2010).
32. S. Kimura and T. Wilson, "Confocal scanning optical microscope using single-mode fiber for signal detection," *Appl. Opt.* **30**(16), 2143–2150 (1991).
33. M. A. Troyanova-Wood and V. V. Yakovlev, "Multi-wavelength excitation Brillouin spectroscopy," *IEEE J. Sel. Top. Quantum Electron.* **27**(4), 1–5 (2021).

34. S. Mattana, S. Caponi, F. Tamagnini, D. Fioretto, and F. Palombo, "Viscoelasticity of amyloid plaques in transgenic mouse brain studied by Brillouin microspectroscopy and correlative Raman analysis," *J. Innov. Opt. Health Sci.* **10**(06), 1742001 (2017).
35. Z. Meng, T. Thakur, C. Chitrakar, M. K. Jaiswal, A. K. Gaharwar, and V. V. Yakovlev, "Assessment of local heterogeneity in mechanical properties of nanostructured hydrogel networks," *ACS Nano* **11**(8), 7690–7696 (2017).
36. Z. Meng, S. C. Bustamante Lopez, K. E. Meissner, and V. V. Yakovlev, "Subcellular measurements of mechanical and chemical properties using dual Raman-Brillouin microspectroscopy," *J. Biophoton* **9**(3), 201–207 (2016).
37. K. Berghaus, J. Zhang, S. H. Yun, and G. Scarcelli, "High-finesse sub-GHz-resolution spectrometer employing VIPA etalons of different dispersion," *Opt. Lett.* **40**(19), 4436–4439 (2015).
38. S. Caponi, D. Fioretto, and M. Mattarelli, "On the actual spatial resolution of Brillouin Imaging," *Opt. Lett.* **45**(5), 1063–1066 (2020).
39. E. J. Peterman, F. Gittes, and C. F. Schmidt, "Laser-induced heating in optical traps," *Biophys. J.* **84**(2), 1308–1316 (2003).
40. C. Ying, E. Karakaci, E. Bermudez-Urena, A. Ianiro, C. Foster, S. Awasthi, A. Guha, L. Bryan, J. List, and S. Balog, "Watching single unmodified enzymes at work," arXiv:2107.06407 (2021).
41. H. Mao, J. R. Arias-Gonzalez, S. B. Smith, I. Tinoco Jr, and C. Bustamante, "Temperature control methods in a laser tweezers system," *Biophys. J.* **89**(2), 1308–1316 (2005).
42. W. M. Lee, P. J. Reece, R. F. Marchington, N. K. Metzger, and K. Dholakia, "Construction and calibration of an optical trap on a fluorescence optical microscope," *Nat. Protoc.* **2**(12), 3226–3238 (2007).
43. J. Rouch, C. Lai, and S. Chen, "Brillouin scattering studies of normal and supercooled water," *J. Chem. Phys.* **65**(10), 4016–4021 (1976).
44. C. L. Chiu, V. Hecht, H. Duong, B. Wu, and B. Tawil, "Permeability of three-dimensional fibrin constructs corresponds to fibrinogen and thrombin concentrations," *BioResearch Open Access* **1**(1), 34–40 (2012).
45. H. Mahmodi, A. Piloni, R. H. Utama, and I. Kabakova, "Mechanical mapping of bioprinted hydrogel models by Brillouin microscopy," *Bioprinting* **23**, e00151 (2021).
46. P. H. J. Kouwer, M. Koepf, V. A. A. Le Sage, M. Jaspers, A. M. van Buul, Z. H. Eksteen-Akeroyd, T. Woltinge, E. Schwartz, H. J. Kitto, R. Hoogenboom, S. J. Picken, R. J. M. Nolte, E. Mendes, and A. E. Rowan, "Responsive biomimetic networks from polyisocyanopeptide hydrogels," *Nature* **493**(7434), 651–655 (2013).
47. Y. Yasuno, V. D. Madjarova, S. Makita, M. Akiba, A. Morosawa, C. Chong, T. Sakai, K.-P. Chan, M. Itoh, and T. Yatagai, "Three-dimensional and high-speed swept-source optical coherence tomography for in vivo investigation of human anterior eye segments," *Opt. Express* **13**(26), 10652–10664 (2005).
48. F. Vetrone, R. Naccache, A. Zamarrón, F. A. Juarraz de la Fuente, L. Sanz-Rodríguez, E. Martínez Maestro, D. Martín Rodríguez, J. Jaque, J. A. García Sole, and Capobianco, "Temperature sensing using fluorescent nanothermometers," *ACS Nano* **4**(6), 3254–3258 (2010).
49. T. Fischer, A. Hayn, and C. T. Mierke, "Fast and reliable advanced two-step pore-size analysis of biomimetic 3D extracellular matrix scaffolds," *Sci. Rep.* **9**, 1–10 (2019).
50. M. Bailey, M. Alunni-Cardinali, N. Correa, S. Caponi, T. Holsgrove, H. Barr, N. Stone, C. P. Winlove, D. Fioretto, and F. Palombo, "Viscoelastic properties of biopolymer hydrogels determined by Brillouin spectroscopy: a probe of tissue micromechanics," *Sci. Adv.* **6**(44), eabc1937 (2020).